Proceedings of the ASME 2010 3rd Joint US-European Fluids Engineering Summer Meeting and 8th International Conference on Nanochannels, Microchannels, and Minichannels
FEDSM-ICNMM2010
August 1-5, 2010, Montreal, Canada

FEDSM-ICNMM2010-30829

Scale-Dependent Energy Fluxes in a Rough-wall Turbulent Channel Flow

Jiarong Hong
Johns Hopkins University
Baltimore, MD, U.S.A

Joseph Katz
Johns Hopkins University
Baltimore, MD, U.S.A

Michael P. Schultz
Naval Academy
Annapolis, MD, U.S.A

ABSTRACT

In this paper, we investigate the characteristics of energy fluxes within rough-wall turbulent boundary layer at different scales in the context of large eddy simulations (LES) utilizing high resolution Particle Image Velocimetry (PIV) data obtained in an optically index-matched facility. The rough surface consists of closely-packed pyramidal elements, and the measurement region includes the entire roughness sublayer and lower portion of outer-layer with a vector resolution of ~9 wall units and 14% of roughness height. Our recent study has demonstrated that the entire boundary layer is flooded with an excessive number of roughness-scale eddies that are generated near the wall and advected away from it by large scale coherent structures present in the outer layer. Following this observation, the original velocity field is spatially filtered using 2D top-hat filter of length scale $\Delta=1k$, $3k$, $6k$ (k is roughness height) that represent roughness, intermediate and large scale motions, respectively. In these ranges, the subgrid scale (SGS) energy fluxes show substantial increase with scale and with decreasing distance from the wall. The latter trend persists even when fluxes are scaled with the local TKE production rate. When the fluxes are decomposed to local and non-local contributions, they show a scale-dependent near-wall increase of energy transfer which bypasses the typical cascading process. This non-local flux is even larger than the local one near the wall for the [k, $3k$] range. These trends are attributed to interactions of large scale turbulence with the wall roughness and the abundant roughness scale eddies near the wall. The paper also examines the behavior of Smagorinsky model coefficients, and show scale-dependence when trends at filter scales of $1k$ and $3k$ are compared to those at $6k$. Both dissipation based and dynamic model coefficients show very little variation with height as long as the filter scale is in the $1-3k$ range, but increase with elevation for $\Delta=6k$.

NOMENCLATURE

k	Roughness height
k_s	Equivalent sand roughness height
λ	Roughness wavelength
Δ	Filter size
C_s	Smagorisky coefficient
h	Half channel height
λ	Boundary layer thickness
λ_v	Viscous length scale
U_λ	Friction velocity
η	Kolmogorov scale
k_1	Streamwise wavenumber
Π	Energy flux
P	Turbulent kinetic energy production rate
ε	Dissipation rate
$E_{ii}(k_1)$	Energy spectra
x, y, z	Streamwise, wall-normal and spanwise directions
u',v',w'	Velocity fluctuation at x, y, z directions
$< >$	Ensample average
$\overline{\quad}$	Spatial average

INTRODUCTION

It is commonly accepted that in smooth-wall turbulent boundary layers, there are two dominant length scales. The integral length scale, typically, the boundary layer thickness λ or half channel height h, governs the outer-layer, large scale motions, while the characteristic length scale of inner layer structures is the viscous length scale λ_v [1]. For a turbulent flow over a hydrodynamically rough surface, interaction of the roughness with large and small scale flow motions introduces length scales associated with the characteristic surface topography.The traditional view of this flow-roughness interaction is based on the wall similarity hypothesis [2], which states outside of the "roughness sublayer", a region extending from the wall up to $2-5k$, turbulent motions in a boundary layer at high Reynolds numbers are independent of wall roughness and viscosity. Jiménez [3] points out that the

Copyright © 2010 by ASME

flow must achieve the so-called "well-characterized" conditions for this hypothesis to be valid, which requires a sufficient scale separation among λ, k and λ_v, typically, $k^+=k/\lambda_v>50–100$, $\lambda/k>40$, $\lambda^+>4000$. Thereafter, a number of experimental studies (e.g. [4-7]) have provided strong support for this hypothesis. For well-characterized rough-wall flows, the impact of roughness on the outer-layer turbulence can be accounted for as a momentum deficit. Nevertheless, in recent experimental study in a rough-wall channel described in Hong *et al.* [8], we have found that although the influence of roughness on turbulence statistics, such as Reynolds stresses, diminishes a few roughness heights above the wall, the roughness still leaves clear imprints in energy and shear spectra in the outer-layer. This influence appears as spectral bumps in the wavenumber range corresponding to the characteristic length scale of the roughness. Based on examination of instantaneous realizations and linear stochastic estimation (LSE) based analysis, we have concluded that these bumps represent excessive presence of roughness-scale eddies, which are produced near the wall and are transported upward by large scale turbulent structures that populated in the outer-layer. Although these eddies have limited contribution to Reynolds stresses compared with large-scale structures, they have a strong influence on the dissipation rate and related dissipation-range variables. This effect is a result of the roughness scales falling in the most dissipative range of a typical Kolmogorov energy spectrum.

Excessive small scale energy may have significant implications in the LES of turbulent flows over rough walls. As a means of bridging the gap between the Reynolds-averaged Navier-Stokes (RANS) simulation that filters the turbulence completely, and direct numerical simulation (DNS) that completely resolves the turbulence, LES simulate the large-scale turbulent motions in a coarse grid and models the influence of small scale eddies ([9-11]). When the grid size used in the LES is too large to resolve the flow-roughness interactions, they must be modeled appropriately, especially the associated depletion of large-scale energy by the unresolved small scales, along with the relationships among roughness geometry, large-scale motions and wall shear stress. Development of such models has proven to be a major challenge to date that has not been resolved even for smooth-wall boundary layers ([9], [12-13]), and appears to be a formidable task for rough walls where the roughness geometry has be accounted for in some way. When the roughness leaves a small-scale signature with significant effect on energy dissipation rate and related quantities over the entire boundary layer, its effect must also be considered. Consequently, it would be beneficial to examine energy fluxes and interactions among them at different scales within the rough-wall boundary layer, and their impact on the SGS stress modeling.

In light of the above discussion, the present study utilizes the abovementioned high resolution PIV data for a rough-wall turbulent channel flow [8] to characterize energy fluxes at length scales and elevations from the rough wall. This database covers the entire roughness sublayer and lower portion of the outer-layer. As the first step, the velocity field is spatially filtered at the scales, which are selected based on the spectral analysis to represent the roughness, intermediate and large scale motions. The measured local and non-local energy fluxes along with the associated dissipation-based and dynamic Smagorinsky model coefficients reveal scale and elevation dependent trends that result, at least in part, from the effect of excessive roughness-generated small scale energy.

Experimental Set-up and Methodology

The experiment is performed in the bypass channel of the JHU index-matched waterjet pump test facility(e.g. [14]), which is illustrated in **Fig. 1**. The entire facility is filled with 62% by weight solution of Sodium Iodide (NaI) in water whose refractive index matches that of the acrylic rough walls. The bypass consists of an independent settling chamber, a converging nozzle, a test section and a diffuser. The acrylic test section is 3.3 m long, and has a 20×5 cm^2 rectangular cross section, facilitating optical access to any internal site from various viewing angles. Two pairs of 1.25 m long removable acrylic inserts enable us to control the wall properties. The rough-wall channel flow is generated with a pair of smooth inserts in the upstream half of the channel, and a pair of rough ones downstream. According to Antonia *et al.* [15], to achieve a self-similar rough-wall boundary layer, one must have a sufficient streamwise fetch with roughness of approximately $15–20\delta$. Therefore, as illustrated in **Fig. 2a**, our measurements are conducted at $35h$ from the leading edge of the downstream insert. The rough surface is composed of closely-packed pyramidal elements, which are illustrated in **Fig. 2**. This type of roughness has well-defined length scales, i.e. its height k and wavelength λ, making it sufficiently simple for performing spatial sampling of data while retaining the 3D nature of the roughness. The individual pyramid in the present study has a height of 0.46 mm and a slope angle of 16° (**Fig. 2c**), resulting in $\lambda\approx7k$. Based on data provided in Schultz *et al.* [16], this roughness has an explicit relation between k_s and k, namely, $k_s\sim1.5k$. As a result, based on the measured friction velocity shown in **Table 1** (from [8]), the rough-wall channel flow yields $h/k=50$ and $k_s^+>80$, satisfying the well-characterized condition, as discussed in Jiménez [3].

PIV Measurements have been conducted in multiple x-y and x-z planes (see coordinates in **Fig. 1**) as well as two different magnifications. Our current study utilizes high resolution x-y plane data located in close proximity to the centerline of the channel, as illustrated in **Fig. 2b**. The full details of data acquisition and velocity vector calculations are described in [8]. The vector maps have a vector spacing of 63μm, corresponding to 9 wall units and $0.138k$. This resolution provides 36 rows of vectors within $5k$ above the index-matched rough surface. In the present paper, the

Copyright © 2010 by ASME

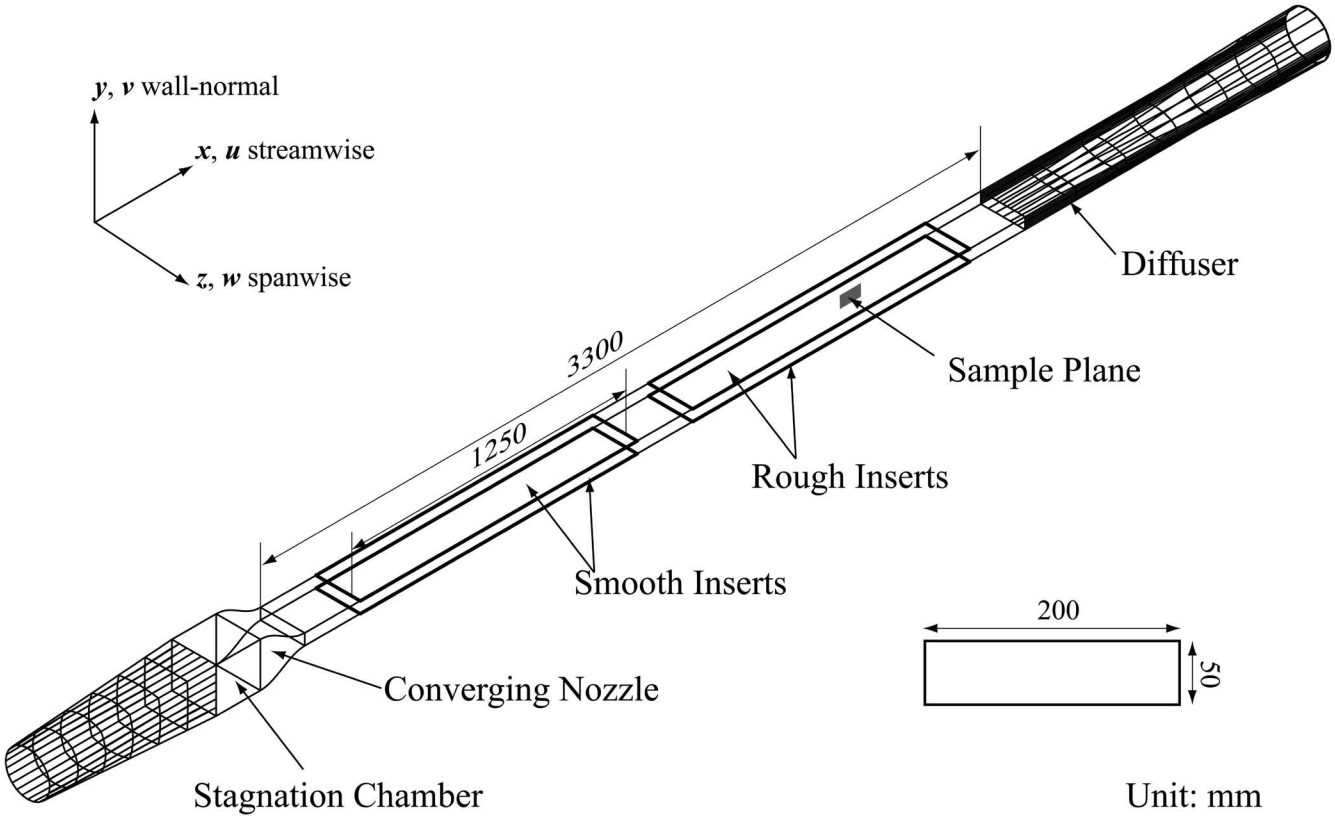

Fig. 1 The bypass channel in the optically index-matched facility.

analysis is carried out starting from the top of roughness elements, where y=0 is placed (**Fig. 2c**). The lowest data point is located at y=36 μm, i.e. y^+~5. Approximately 5000 instantaneous velocity distributions are obtained at this sample plane to achieve reasonable convergence of turbulence statistics.

The flow conditions and relevant parameters for the present study are listed in **Table 1**. The magnitude of Re_h is calculated using the half channel height and centerline velocity, while Re_λ is based on the friction velocity U_λ, whose value is evaluated using two approaches. The value of $U_{\lambda\text{-}log}$ is determined by a logarithmic fit to the mean velocity profile in y=2k–0.2h. The slope of a linear least-square-fit to the total shear stress, i.e. the sum of viscous and Reynolds shear stresses, is used for obtaining $U_{\lambda\text{-}uv}$. As is evident, the present values of $U_{\lambda\text{-}log}$ and $U_{\lambda\text{-}uv}$ are very close. Typically (e.g. [17]), $U_{\lambda\text{-}log}$ is employed for analysis of trends in mean velocity distributions, while $U_{\lambda\text{-}uv}$ is used for scaling Reynolds stresses. In **Table 1**, the value of Re_λ is calculated based on $U_{\lambda\text{-}uv}$.

SGS FLUX AND SGS STRESS MODELS

LES decomposes the flow variables into resolved and unresolved (subgrid scale) part by applying a spatial filtering operation ([9-11], [18]). The filtered variable is given by $\tilde{f} = \int_D f(\vec{x}',t)G_\Delta(\vec{x},\vec{x}')d\vec{x}'$, where D is the computational domain and G_Δ is the filtering kernel that has a characteristic scale Δ. The filtered velocity satisfies the Navier-Stokes equation

$$\frac{\partial \tilde{u}_i}{\partial t} + \tilde{u}_j \frac{\partial \tilde{u}_i}{\partial x_j} = -\frac{\partial}{\partial x_j}\left[\frac{\tilde{p}}{\rho}\delta_{ij} + \tau_{ij}\right] + \nu \frac{\partial^2 \tilde{u}_i}{\partial x_j^2}, \quad (1)$$

where $\tau_{ij} = \widetilde{u_i u_j} - \tilde{u}_i \tilde{u}_j$ is the SGS stress. Analysis of energy budget shows that the energy transfer between resolved and unresolved scales is

$$\Pi_\Delta = -<\tau_{ij}\tilde{S}_{ij}>, \quad (2)$$

where $\tilde{S}_{ij} = 0.5(\partial\tilde{u}_i/\partial x_j + \partial\tilde{u}_j/\partial x_i)$ is the filtered strain rate tensor. It is commonly referred to as SGS energy flux, and appears as a sink term in the kinetic energy equation of filtered velocity and a source in the balance equation of subgrid kinetic energy. The SGS stress has to be modeled to close the filtered momentum equation system. Among the numerous models proposed to approximate SGS stresses using resolved flow variables, the present study select two popular models, namely the static Smagorinsky eddy viscosity [19], andthe traditional dynamic model ([20], [21]). Both of them are based on an assumption that

$$\tau_{ij}^d = -2\nu_T \tilde{S}_{ij}, \nu_T = (C_S\Delta)^2|\tilde{S}|, \quad (3)$$

Copyright © 2010 by ASME

U_c m/s	Re_h	k mm	k_s^+	$U_{\lambda\text{-}log}$ m/s	$U_{\lambda\text{-}uv}$ m/s	Wall unit μm	Re_λ
2.75	62500	0.46	95	0.159	0.155	7.1/7.3	3520

Table 1: Experimental Flow Conditions

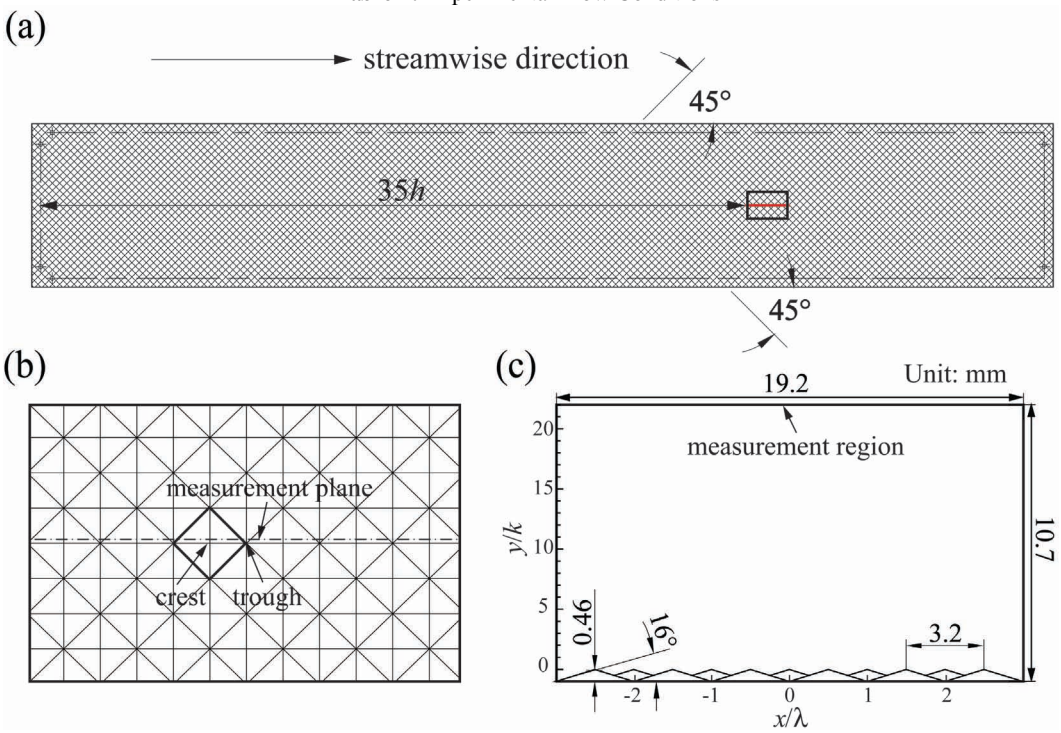

Fig. 2 (a) The rough surface plate and the location of measurement plane (marked with a red solid line). (b) A magnified view of the rectangular area marked by solid lines in (a), showing the relative position of measurement plane to pyramidal elements.The solid square marks an individual pyramid. (c) An *x*-*y* plane projection of wall roughness andthe measurement plane.

where $\tau_{ij}^d = \tau_{ij} - 1/3 \cdot \tau_{kk}\delta_{ij}$ is the deviatoric part of SGS stress tensor, ν_T is the SGS eddy viscosity, $|\tilde{S}| = (2\tilde{S}_{ij}\tilde{S}_{ij})^{0.5}$, and C_s is the Smagorinsky coefficient. In the static (or dissipation based) model, C_s is calculated by matching the real and modeled SGS energy fluxes, i.e.

$$(C_S)^2 = \Pi_\Delta / < 2\Delta^2 \,|\, \tilde{S} \,|\, \tilde{S}_{ij}\tilde{S}_{ij} > , \tag{4}$$

where $< >$ indicates ensemble averaging. This coefficient guarantees the correct mean depletion of energy from the resolved velocity field, and Eqn.4 can be employed to evaluate the Smagorinsky coefficients for various flow fields. For homogeneous and isotropic turbulence, $C_s \approx 0.16$ (Lilly [22]). In the dynamic model, the coefficients are calculated dynamically and locally during the LES (which has a resolution of Δ) by filtering the simulated data at a scale $\alpha\Delta$, and determining C_s from,

$$C_S^{\Delta,\,\mathrm{DM}} = < L_{ij}M_{ij} > / < M_{ij}M_{ij} > , \tag{5}$$

$$L_{ij} = \overline{\tilde{u}_i\tilde{u}_j} - \bar{\tilde{u}}_i\,\bar{\tilde{u}}_j , \tag{6}$$

$$M_{ij} = -2\tilde{\Delta}^2(\alpha^2 \,|\, \bar{\tilde{S}} \,|\, \bar{\tilde{S}}_{ij} - \overline{|\tilde{S}|\,\tilde{S}_{ij}}) , \tag{7}$$

where the overbar indicates spatial filtering at a scale $\alpha\Delta$. A number of studies, e.g. [23], [24], have been carried out to evaluate the performance of SGS models based on 2D PIV data. The analysis procedure in our paper follows the guidance provided in Liu *et al.* [23]. A 2D top-hat filter is employed to spatially filter the velocity field, and the spatial derivatives are obtained using the 2nd order finite differencing on a coarse grid of filter size. Since we do not have 3D data to calculate all the required tensor components, the contractions are approximated by their 2D surrogates, namely,

$$\Pi_\Delta^{2d} = -\left(< \tau_{11}\tilde{S}_{11} > + < \tau_{22}\tilde{S}_{22} > + 2 < \tau_{12}\tilde{S}_{12} > \right), \tag{8}$$

$$|\tilde{S}^{2d}|^2 = 2(\tilde{S}_{11}\tilde{S}_{11} + \tilde{S}_{22}\tilde{S}_{22} + 2\tilde{S}_{12}\tilde{S}_{12}) , \tag{9}$$

The rest of the variables introduced in Eqns**.** 4-7 are calculated in the same way and denoted with the superscript 2d. In some of the analysis presented in this paper, to calculate energy fluxes and coefficients, we first obtain ensemble-averaged data at each point based on the 5000 realizations, and then spatially average the result along horizontal lines, each consisting of 100 data points and covering about 2λ. This process achieves better statistical convergence but eliminates the spatial variability occurring in the roughness sublayer, which is beyond the present scope [8].

Copyright © 2010 by ASME

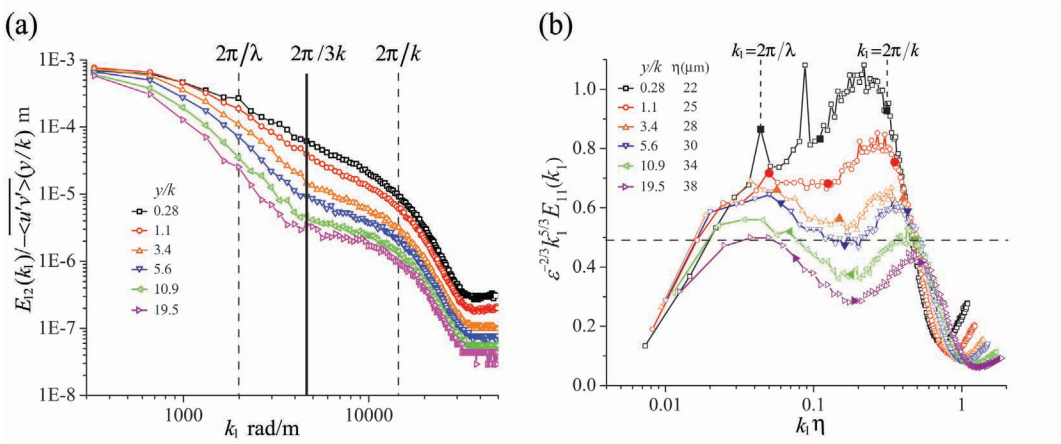

Fig. 3 (a) Spatial shear spectra $E_{12}(k_1)$ scaled by the local shear stress. The vertical solid line marks the approximate wavenumber that separates the roughness scale from the large scale turbulence. The dashed lines marks the wavenumbers corresponding to roughness height and roughness wavelength. (b) Compensated energy spectra of $E_{11}(k_1)$, with magnified solid symbols marking wavenumbers corresponding to length scale of$k$, $3k$ and λ. The horizontal dashed line represents the value of compensated spectrum for inertial-range isotropic turbulence [8].

RESULTS

In [8], we have observed that the spatial turbulent energy and shear spectra flatten and develop bumps in wavenumbers corresponding to 1−3k. Two sample spectra from this study are provided in **Fig. 3.** The spatial shear spectra (**Fig. 3a**) are scaled by the spatially-averaged Reynolds stress at the corresponding elevation, which keeps both horizontal and vertical axes dimensional. This scaling emphasizes subtle variations in spectral shapes with increasing distance from the wall. The compensated spectra $E_{11}(k_1)\varepsilon^{-2/3}k_1^{5/3}$ (**Fig. 3b**) are plotted against $k_1\eta$, where Kolmogorov scale is estimated based on dissipation rate at the corresponding elevation, i.e. $\eta=\left(\nu^3/\varepsilon(y)\right)^{0.25}$. Accordingly, since ε decays with increasing elevation, values of $k_1\eta$ corresponding to a certain length scale, e.g. k or λ, share the same trend. For the purpose of completeness, it is worth reviewing some of the observed spectral features. First, the spectral peak at $k_1=2\pi/\lambda$ very near the wall is generated by the periodic spatial variations in the flow within the roughness sublayer. Secondly, at low wavenumbers, the spectral slope in **Fig. 3a** steepens with increasing distance from the wall, demonstrating a growing contribution of large-scale turbulence, and decreasing role of small-scale energy. Thirdly, at low wavenumbers of higher elevations in the outer-layer, the shear spectra show a tendency towards a −7/3 slope, the expected value for the inertial-range shear spectrum [25]. Finally, a clear flattening pattern, i.e. a decrease in slope magnitude with increasing distance from the wall, is observed for wavelengths in the 1−3k range.This feature is most pronounced in the presented shear spectra but is also evident in the energy spectra, appearing as distinct bump in the compensated ones (**Fig. 3b**). It occurs at all elevations, including well above the roughness sublayer, and indicate presence of excessive energy at this scale range.

In general, the entire compensated $E_{11}(k_1)$ decreases rapidly with elevation, with a particularly fast decay rate around the high wavenumber bump. Above the roughness sublayer, another peak forms at low wavenumbers of the compensated $E_{11}(k_1)$ in the vicinity of $k_1\eta$~0.04, and its magnitude tends towards the value of compensated spectrum for inertial-range isotropic turbulence, which is marked by a dashed line in **Fig. 3b**. This two-peak structure for the compensated spectra is associated with structures developed at the two ends of the rough wall boundary layer. The low wavenumber peak corresponds to the inertial-range structures of the outer-layer, while the high wavenumber peak is associated with roughness-scale eddies generated very near and amid the roughness elements. There are also clear troughs between the two spectral peaks in the compensated spectra. Outside of the roughness sublayer, the troughs seem to fall at approximately the same $k_1\eta$, but they also almost coincide with the wavenumber corresponding to $3k$. The latter are marked as a solid vertical line in **Fig. 3a** and magnified solid symbols in **Fig. 3b**. Based on this observation, we choose three length scales of size $\Delta=1k$, $3k$, $6k$ to filter the original velocity field. With this logic, we divide the flow field into four scale ranges, i.e. sub-roughness scale, roughness scale range (1−3k), intermediate scale (3−6k), large scale range (>6k). The roughness-scale (bandpass filtered) range is obtained by subtracting filtered vector maps at scale k and $3k$ from each other. It highlights turbulent flow structures associated with the characteristic length scale of roughness, which contributes to the formation of compensated spectral peak at high wavenumber range. The same procedure can be implemented for examining the intermediate scale range, and filtering $6k$ reserves only inertial and large-scale turbulent structures, which are responsible for the low wavenumber peaks in the compensated spectra.

Copyright © 2010 by ASME

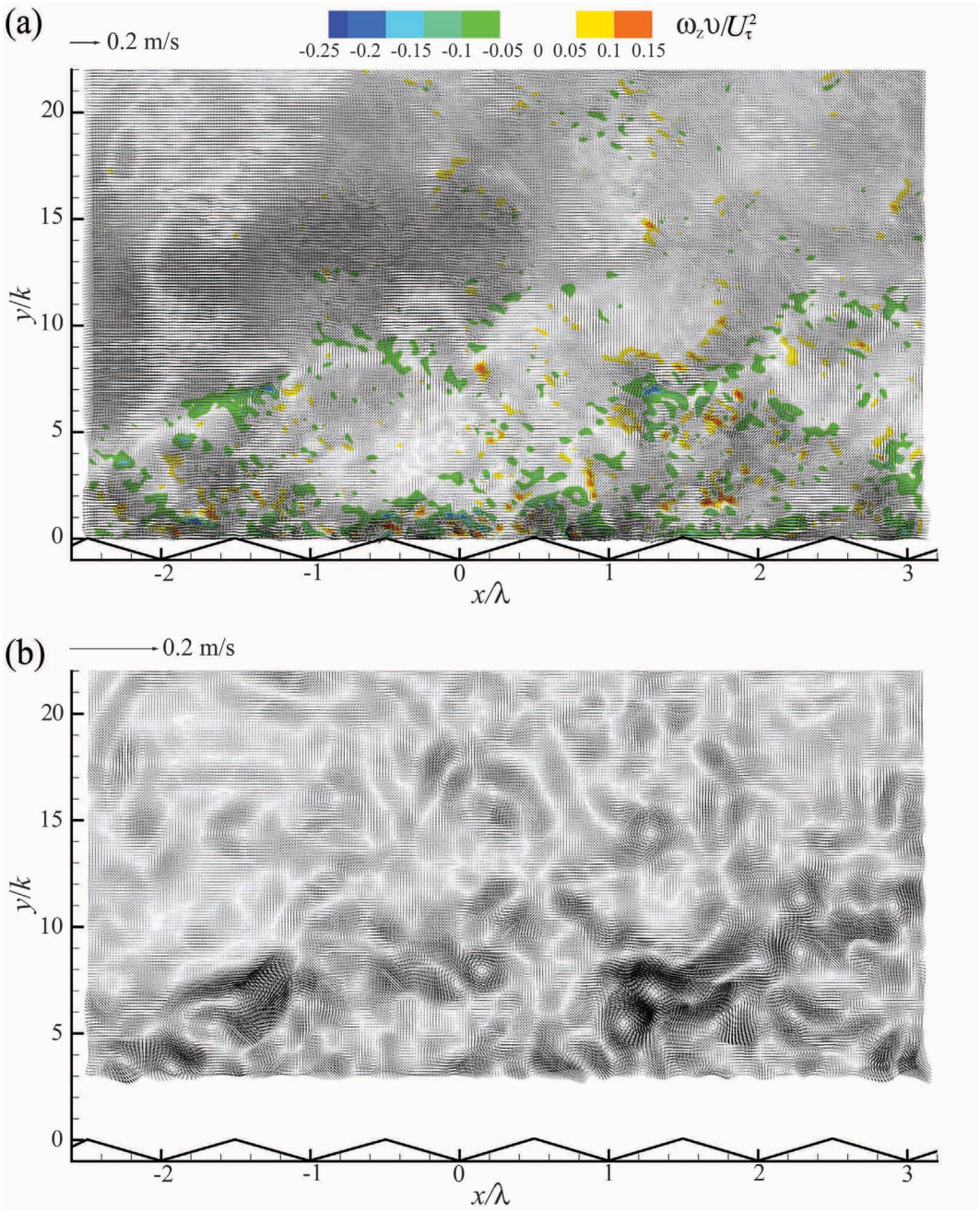

Fig. 4 (a) A sample of instantenous vector map after subtracting $0.6U_c$ from each vector. Colors indicate the scaled vorticity. (b) The same velocity field, spatially bandpass filtered using top-hat filters in the $1k$-$3k$ range.

Features of large-scale, outer-layer structures and roughness-scale eddies can be observed by bandpass filtering of instantaneous realizations. **Fig. 4** shows a sample of Galilean-translated original (**Fig. 4a**) and roughness-scale range velocity field (**Fig. 4b**). In **Fig. 4a**, two inclined large scale structures of about the same scale are observed. Both of them extend from $y \approx 3k$ to $10k$, in the elevation range where the two-peak compensated spectral pattern emerges. Each one has a 2D signature that resembles the hairpin structures studied by Adrian's group (e.g. [26]). The spacing between the two is $2-3\lambda$, which roughly corresponds to the length scale of the low wavenumber peak in **Fig. 3b**. The region below this structure is heavily populated with small scale eddies. Adjacent the roughness, the flow contains several inclined trains of small vortices. As expected, in the bandpass-filtered map (**Fig. 4b**), the entire field is filled with eddies in the [k, $3k$] size range. However, the signature of large scale structures is marked by clear spatial variation in the strength of roughness-scale eddies. Within the large structures, the vortical motions are stronger and appear to be associated with "newborn" eddies that have just been entrained from the wall. Further above, the roughness-scale structures are relatively

Copyright © 2010 by ASME

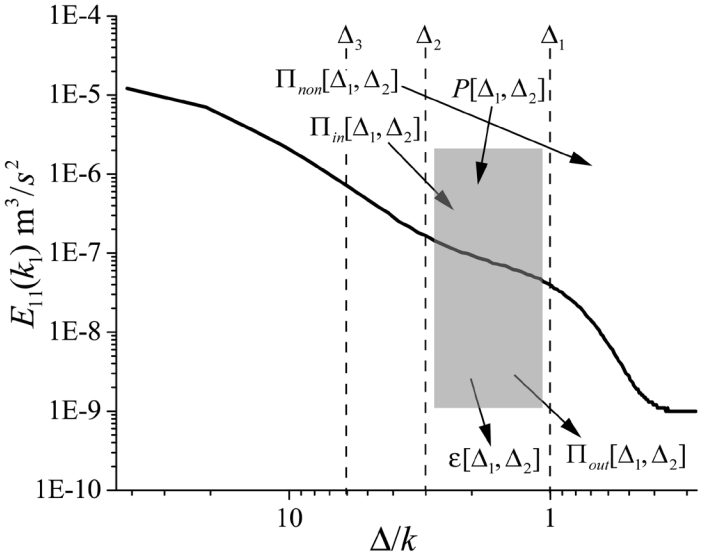

Fig. 5 A schematic showing turbulent energy fluxes into, out of, and bypassing the scale range [Δ_1, Δ_2] along with the production and dissipation rates in this scale range. In the present study, the three dashed vertical bars from left to right correspond to $\Delta_1=k$, $\Delta_2=3k$, $\Delta_3=6k$, respectively.

weak, presumably since they have been entrained at earlier times, and have partially dissipated. Similar patterns, with variation in size and location, are present in numerous instantaneous velocity distributions that we have examined, indicating that the anecdotal evidence shown here is a regularly occurring phenomenon. Since the time scale associated with the vertical transport is not long enough for these eddies to dissipate, they leave imprints in the spectra across the entire flow domain. Clearly, these eddies are not produced by the typical energy cascading process starting from turbulence at large scales, and hence lead to distinct bumps in the compensated spectra (**Fig. 3b**).

To quantitatively understand the interaction among the small and large scale structures, we use Π_Δ to represent the total energy flux across each filter scale Δ. Considering two filters of size Δ_1 and Δ_2 ($\Delta_2 > \Delta_1$), the energy flux across Δ_2 can be decomposed into two components:

$$\Pi_{in}[\Delta_1,\Delta_2] = -L_{ij}\tilde{\bar{S}}_{ij}\,, \tag{10}$$

$$\Pi_{non}[\Delta_1,\Delta_2] = -\bar{\tau}_{ij}\tilde{\bar{S}}_{ij}\,, \tag{11}$$

where ~ and overbar represent filtering at Δ_1 and Δ_2, respectively (Δ_2 is equivalent to $\alpha\Delta_1$ in Eqns. 5–7). Following [24], $\Pi_{in}[\Delta_1,\Delta_2]$ is the so-called 'local' energy flux from scales above Δ_2 to the [Δ_1, Δ_2] range, while $\Pi_{non}[\Delta_1,\Delta_2]$ is the 'not-so-local' contribution, i.e. the energy flux bypassing the [Δ_1, Δ_2] range. **Fig. 5** illustrates three energy flux terms related to [Δ_1, Δ_2], where $\Pi_{out}[\Delta_1,\Delta_2]$ is the energy cascading down from [Δ_1, Δ_2] to smaller scales. It is calculated using

$$\Pi_{out}[\Delta_1,\Delta_2] = \Pi_{\Delta_1} - \Pi_{non}[\Delta_1,\Delta_2]\,, \tag{12}$$

For the [Δ_1, Δ_2] range, the energy balance is

$$\Pi_{in}[\Delta_1,\Delta_2] + P[\Delta_1,\Delta_2] = \Pi_{out}[\Delta_1,\Delta_2] + \varepsilon[\Delta_1,\Delta_2]\,, \tag{13}$$

where $P[\Delta_1,\Delta_2]$ and $\varepsilon[\Delta_1,\Delta_2]$ are the local energy production and dissipation within [Δ_1, Δ_2]. For our targeted scale ranges [k, 3k] and [3k, 6k], we assume that the local energy production is negligible compared with dissipation, consistent with trends of shear spectra outside the roughness sublayer. Therefore, the difference between energy fluxes into and out of these scale ranges is assumed to be equal to the amount of energy being dissipated. Accordingly, we introduce dissipation efficiency

$$\eta = (\Pi_{in}[\Delta_1,\Delta_2] - \Pi_{out}[\Delta_1,\Delta_2]) / \Pi_{in}[\Delta_1,\Delta_2]\,, \tag{14}$$

which quantifies how dissipative the turbulence in the [Δ_1, Δ_2] range is.

Mean SGS fluxes at $\Delta=k$, 3k, 6k are illustrated in **Fig. 6a** along with the streamwise spatially-averaged production and dissipation rates. All the quantities presented are 2D surrogates based on the x-y plane data, where

$$\varepsilon^{2d} = <(\partial u'/\partial x)^2 + (\partial u'/\partial y)^2 + (\partial v'/\partial x)^2 + (\partial v'/\partial y)^2>\,, \tag{15}$$

$$P^{2d} = -<u'v'>\partial<u>/\partial y\,, \tag{16}$$

The magnitude of ε^{2d} is 1/3~7/15 (depending on the distance from the wall) of the total estimated dissipation in [8], where the 2D values are extended to 3D using isotropic turbulence assumption. P^{2d} is simply the shear production term, and represent most of the total TKE production rate after spatial averaging [8]. Before discussing trends, it should be pointed out that dissipation shown in **Fig. 6a** is underestimated due to the limited spatial resolution of the PIV measurements, especially near the wall, and therefore falls below the SGS fluxes. It is also evident that all the mean SGS fluxes follow a

Copyright © 2010 by ASME

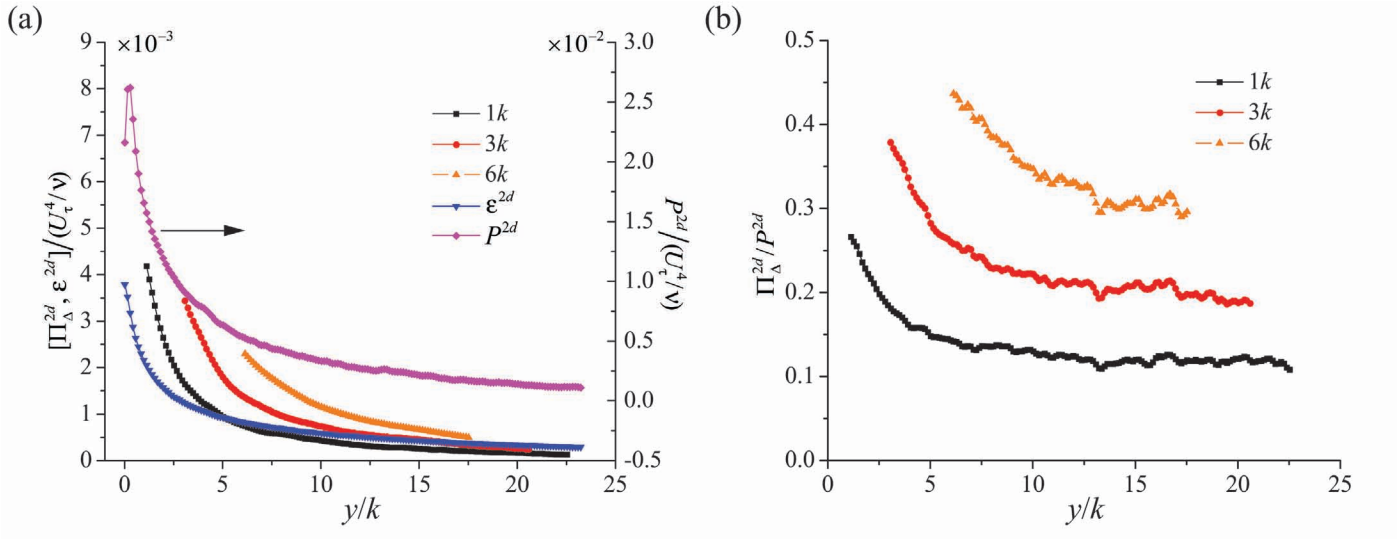

Fig. 6 (a)Mean 2D surrogates for SGS energy fluxed for filter scales $\Delta=1k$, $3k$, $6k$ along with the 2D TKE production and dissipation rates; and (b) The SGS fluxes scaled by the local 2D production rates.

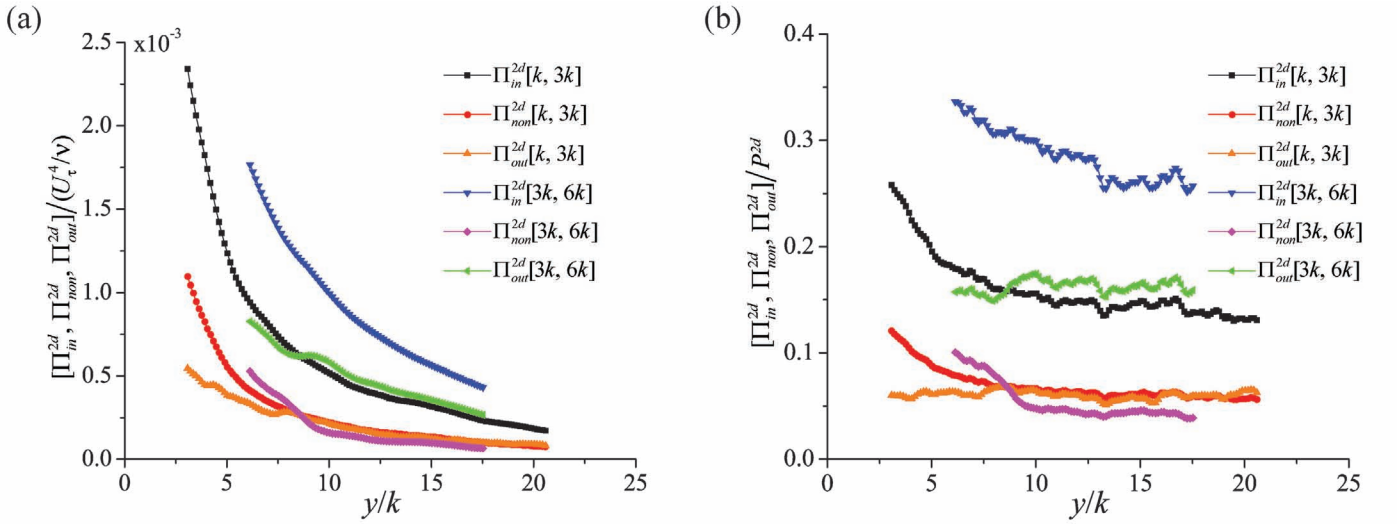

Fig. 7 Turbulent energy into, out of and bypassing scale ranges $[k, 3k]$ and $[3k, 6k]$ scaled by (a) U_τ^4/ν , and (b) P^{2d}.

similar trend as the production and dissipation rates, namely they increase rapidly as the wall is approached. For the same elevation, the flux increases with increasing of filter scales, and the discrepancy among scales escalates with decreasing distance from the wall, indicating increasing dissipation within each present scale range. The higher SGS fluxes are likely associated with the upsurge of TKE production in the inner region. However, when the mean SGS energy fluxes are scaled with the production rate at each elevation (**Fig. 6b**), the scaled fluxes still yields an increasing trend, although they do not vary much with elevation in the outer-layer.

To further elucidate this phenomenon, we calculate the energy fluxes into, out-of and bypassing the $[k, 3k]$ and $[3k, 6k]$ ranges (**Fig. 7a)**. In general, the energy fluxes into and out of the $[3k, 6k]$ range are larger than those of $[k, 3k]$, presumably due to the dissipation within these scale ranges. However, one should also keep in mind that some of the difference is a result of unequal band widths of two studied ranges. Decomposition of Π_Δ into the local component $\Pi_{out}[\Delta, \alpha\Delta]$ and the non-local component $\Pi_{non}[\Delta, \alpha\Delta]$ introduces intriguing trends: For $\Delta=1k$, $\alpha=3$, $\Pi^{2d}_{non}[k,3k]$ grows significantly faster than $\Pi^{2d}_{out}[k,3k]$ near the wall, but they have the same magnitude in the outer-layer. Conversely, for $\Delta=1k$, $\alpha=2$, the non-local flux $\Pi^{2d}_{non}[3k,6k]$ is much smaller than the corresponding local flux $\Pi^{2d}_{out}[3k,6k]$ over the entire investigated channel span. Furthermore, when the energy fluxes are scaled with corresponding production rates (**Fig. 7b**), both local fluxes remain almost constant with varying elevations, while the non-local ones still increase near

Copyright © 2010 by ASME

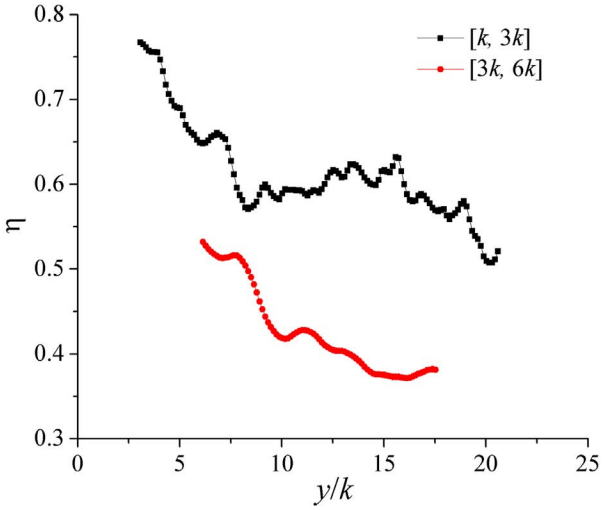

Fig. 8 Dissipation efficiency at scale ranges [k, 3k] and [3k, 6k].

the wall. As it follows, the non-local flux can be regarded as the only contributor to the near-wall increase of scaled SGS energy flux shown in **Fig. 6b**. These trends represent statistical manifestation of two key phenomena occurring in the rough wall boundary layer. First, within the inner part of the boundary layer, interactions of large scale flow structures with the roughness itself, and the abundant roughness-scale eddies induces non-local effects, i.e. direct transfer of energy from large to small scales, which bypasses the local inertial-type cascading process. An energy bypass mechanism has already been discussed by Finnigan [27] for turbulence over plant canopies, where aerodynamic drag on the foliage causes a 'spectral short cut', which removes energy directly from large to fine scales. Presumably, the present flow-roughness interaction bears certain resemblance with phenomena occurring in canopy flows. Second, when the filter scale falls above that of the roughness scale eddies, the non-local effects diminish relative to local ones. Clearly, non-local interactions are more significant contributors to the total SGS energy flux when roughness-scale eddies are involved.

Although the magnitudes of energy dissipated in the [k, 3k] and [3k, 6k] ranges are close (not shown), the dissipation efficiency (**Fig. 8**) shows that the turbulence in the [k, 3k] range is substantially more dissipative than that in [3k, 6k] range. Both efficiency curves remain relatively constant in the outer-layer, but increase rapidly near the wall. In the roughness-scale range, the dissipation efficiency is high everywhere. Especially near the wall, more than 70% of the energy influx is dissipated. This trend is expected since the Kolmogorov scale in the present boundary layer varies from 20 μm near the wall to about 40 μm in the outer layer, the roughness scales fall within the dissipation range and are located in the most-dissipative range near the wall (~20η based on model dissipation spectrum for isotropic turbulence [1]).

Dissipation based Smagorinsky coefficients are calculated at Δ=k, 3k, 6k, and results are compared with static and standard dynamic model coefficients (**Fig. 9a**). In all cases, the dissipation based coefficients are only slightly larger than the isotropic turbulence value of 0.16. For Δ=k and 3k, C_s^k remains about constant across the entire investigated region of the channel, although at 3k, there are signs that C_s^{3k} starts decreasing near the wall. Conversely, C_s^{6k} shows an appreciable rise with elevation. The dynamic model coefficient for Δ=k and test filter at 3k, i.e. $C_s^{DM}(k, 3k)$ in **Fig. 9**, has slightly lower magnitude but shows the same trend as C_s^{3k}. Compared with C_s^{6k}, $C_s^{DM}(3k, 6k)$ also share the similar trend, but its magnitude is higher by ~20%.

Since the calculation of Smagorinsky coefficients involves high order moments of strain rate, the results are sensitive to the numerical approximation of derivatives. To demonstrate this effect, we also calculate the Smagorinsky coefficients using the original fine grid spacing (**Fig. 9b**). It should be pointed out that this estimation does not truly reproduce numerical procedure carried out during LES since such data is not available during the simulations [23]. The fine grid results are for the most part lower than those calculated using a coarse grid, and even slightly below the isotropic turbulence value. Except for $C_s^{DM}(3k, 6k)$, the other coefficients show very little variation with elevation. Although there is some disparity of trends from those in **Fig. 9a**, the fine grid results still yield the observation that filtering below 3k exhibits almost a constant Smagorinsky coefficient in large portion of the boundary layer, while at 6k results in spatial variability. The values of C_s^{Δ} obtained in the fine-grid calculations are closer to those from LES of the atmospheric boundary layer using standard dynamic models (Porté-Angel *et al.*[28]). In their case, C_s increases from 0.02 very near the wall to a constant ~0.13 in the outer-layer.

CONCLUSIONS

As a continuation of our effort to resolve the turbulence within the inner part of rough-wall channel flow, the present work employs spatial filtering and LES related data analysis tools to examine energy transfer across three specific scales, i.e. Δ=1k, 3k, 6k. They categorize the flow field into four ranges of interest, denoted as sub-roughness (<k), roughness (1–3k), intermediate (3–6k) and large (>6k) scale ranges. The mean SGS energy fluxes (across Δ=1k, 3k, 6k) show substantial increase with scale and with decreasing distance from the wall. The latter trends persists even when fluxes are scaled with the TKE production rate at corresponding elevation. Decomposition of the flux into local and non-local contributions shows an intriguing spatial variability and scale dependence of non-local flux which bypasses the typical

Copyright © 2010 by ASME

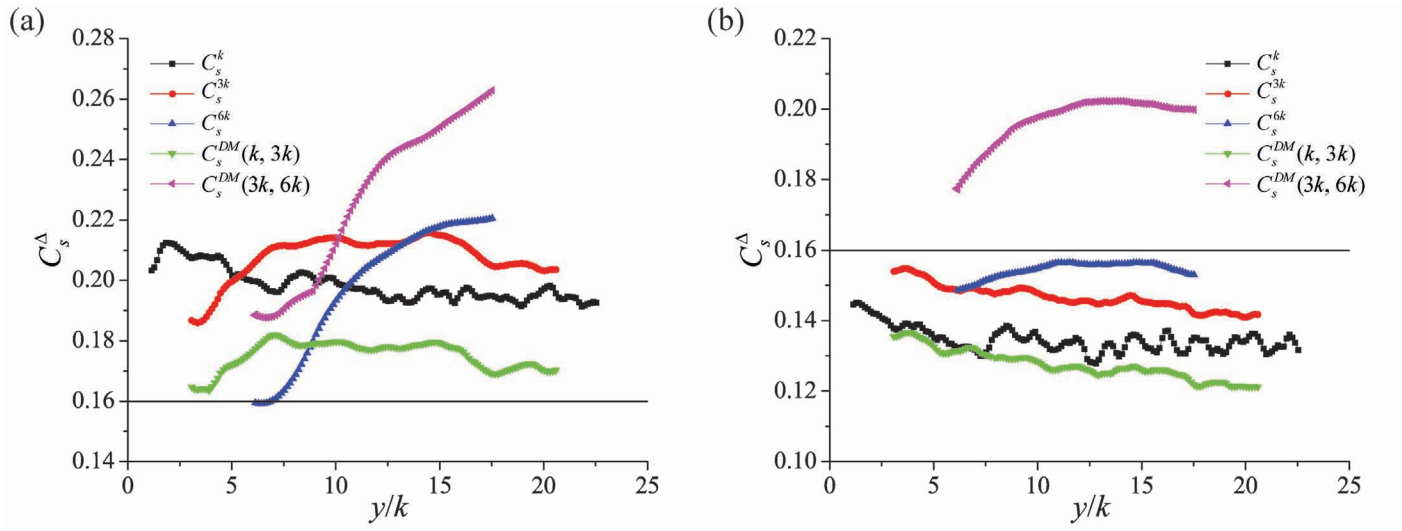

Fig. 9 Dissipation-based Smagorinsky model coefficients (Equ. 4) and Standard dynamic model coefficients (Equ. 5) for several filter scales. The solid horizontal line C_s^Δ=0.16 corresponds to the static Smagorinsky coefficient for homogenous, isotropic turbulence. Results are obtained using derivatives based on (a) coarse grids, and (b) fine girds.

cascading process. When scaled with TKE production, the non-local flux still exhibits a salient near-wall increase while the local one varies little with elevation. Additionally, it is much larger than the local one near the wall for the [k, 3k] range, but becomes significantly smaller in the [3k, 6k] range. These trends are attributed to interactions of large-scale turbulence with the wall roughness and the abundant roughness-scale eddies near the wall. These roughness-scale eddies are also advected rapidly away from the wall by large-scale coherent structures, and flood the entire channel.

This paper also utilizes the experimental data to examine the behavior of Smagorinsky model coefficients. Results show scale-dependence in both dissipation based and dynamic model coefficients when trends at filter scales of 1k and 3k are compared to those at 6k. Both coefficients show very little variation with height as long as the filter scale is in the 1–3k range, but increase with elevation for Δ=6k. These trends suggest that different modeling approaches should be applied when the LES is performed using a grid size of the order of roughness height as compared LES using coarser grids that filter out the effects of the roughness scale eddies.

ACKNOWLEDGMENTS

This research has been funded by Office of Naval Research under grant No. N00014-06-1-0650. The program officer is Ronald Joslin. Construction of the optically index-matched facility has been funded by ONR, in part under grant No. N00014-06-1-0160, and in part by DURIP grant No.N00014-06-1-0556. The program officer is Ki Han Kim.

REFERENCES

[1] Pope S.B. 2000 Turbulent Flows, Cambridge Press.
[2] Raupach M.R., Antonina R.A. & Rajagopalan S., 1991, “Rough-wall turbulent boundary layers”, Appl. Mech. Rev. **44**, 1-25.
[3] Jiménez J. 2004, “Turbulent flows over rough walls,” Annu. Rev. Fluid Mech. **36**, 173-196.
[4] Shockling M.A., Allen J.J. & Smits A.J., 2006, “Roughness effects in turbulent pipe flow,” J. Fluid Mech. **564**, 267≈285.
[5] Wu Y. & Christensen K.T., 2007, “Outer-layer similarity in the presence of a practical rough-wall topography,”Phys. Fluids **19**, 085108.
[6] Schultz M.P. &Flack, K.A., 2007, “The rough-wall turbulent boundary layer from the hydraulically smooth to the fully rough regime”J. Fluid Mech. **580**, 381-405.
[7] Volino R.J., Schultz M.P. & Flack K.A., 2009,“Turbulence structure in a boundary layer withtwo-dimensional roughness,” J. Fluid Mech.**635**, 75–101.
[8] Hong J., Katz J. & Schultz P.M., 2010, “Near-wall turbulence statistics and flow structures over 3D roughness in a turbulent channel flow,” J. Fluid Mech. *submitted*.
[9] Piomelli U, 1999, “Large-eddy simulation: achievements and challenges,” *Prog. Aerosp.Sci.* **35**:335–62.
[10] Meneveau C. &Katz J.,2000, “Scale-invariance and turbulence models for large-eddy simulation,” Annu. Rev. Fluid Mech.**32**:1-32
[11] Rogallo, R., & Moin, P., 1984, “Numerical Simulation of Turbulent Flows,” Annu. Rev. Fluid Mech., **16**, p. 99.
[12] Piomelli U. & Balaras E., 2002, “Wall-layer models for large-eddy simulations,” Annu. Rev. Fluid Mech. **34**, 349-374.

Copyright © 2010 by ASME

[13] Cabot WH, 1995,“Large-eddy simulations with wall models,” *Annu. Res. Briefs—1995*, pp.41–50. Center Turbul. Res., Stanford Univ., Calif.
[14] Uzol O., Chow C.Y., Katz J. & Meneveau C., 2002, “Unobstructed PIV measurements within an axial turbo-pump using liquid and blades with matched refractive indices,” Exp. Fluids **33**, 909-919.
[15] Antonia R.A. & Luxton R.E., 1971, “The response of a turbulent boundary layer to a step change in surface roughness. Part 1: Smooth to rough,” J. Fluid Mech. **48**, 721.
[16] Schultz M.P. & Flack, K.A., 2009, “Turbulent boundary layers on a systematically varied rough wall,”Phys. Fluids **21**, 015104.
[17] Bigillon F., Niño Y. & Garcia M.H., 2006, “Measurements of turbulence characteristics in an open-channel flow over a transitionally-rough bed using particle-image velocimetry,” Exp. Fluids **41**, 857
[18] Lesieur, M., & Metais, O., 1996, “New trends in large-eddy simulations of turbulence,” Annu. Rev. Fluid Mech., **28**, pp. 45–82.
[19] Smagorinsky, J., 1963, “General circulation experiments with the primitive equations,” Mon. Weather Rev. **91**, 99-164.
[20] Germano, M. & Piomeeli, U., 1991, “A Dynamic Subgrid-Scale Eddy Viscosity Model,” Physica A, **3**, pp. 1760–1765.
[21] Lilly, D. K., 1992, “A proposed modification of the Germano subgrid-scale closure method,” Phys. Fluids A, **4**, pp. 633–635.
[22] Lilly, D. K., 1967, “The Representation of Small-Scale Turbulence in NumericalSimulation Experiments,” in Proc. IBM Scientific Computing Symp. Environ.Sci., p. 195.
[23] Liu, S., Meneveau, C., & Katz, J., 1994, “On the properties of similarity subgrid-scale models as deduced from measurement in turbulent Jet,” J. Fluid Mech., **275**, 83–119.
[24] Chen, J., Meneveau, C., & Katz, J., 2005, “The implication of mismatch between stress and strain-ratein turbulence subjected to rapid straining and destraining on dynamic LES models,” Trans. ASME I: J. Fluids Engng. **127**, 840–850.
[25] Lumley J.L., 1967, “Similarity and the turbulent energy spectrum,” Phys. fluids **10**, 855-858.
[26] Adrian R.J., Meinhart C.D. & Tomkins C.D., 2000, “Vortex organization in the outer region of the turbulent boundary layer,” J. Fluid Mech. **422**, 1–54.
[27] Finnigan J.J., 2000, “Turbulence in plant canopies,” Annu. Rev. Fluid Mech. **32**, 519–571.
[28] Porté-Agel, F., Meneveau, C., & Parlange, M., 2000, “A scale-dependent dynamic model for large-eddy simulation: application to a neutral atmospheric boundary Layer,” J. Fluid Mech., **415**, 261–284.

Copyright © 2010 by ASME